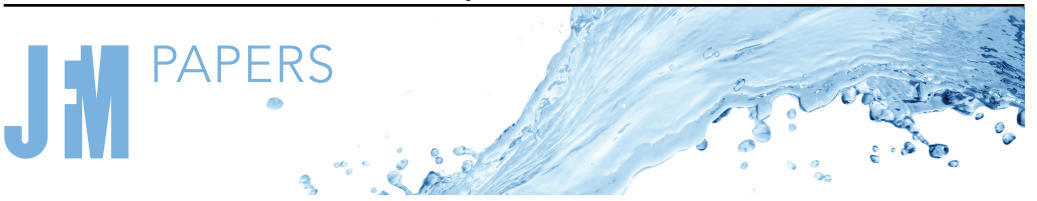
J. Fluid Mech. (2026), *vol.* 1034, A10, doi:10.1017/jfm.2026.11482



Unstable Rossby waves over bathymetry

Joseph Henry LaCasce[1], **Hennes Hajduk**[1,2] **and Jostein Brændshoi**[1,3]

[1]Department of Geosciences, University of Oslo, Norway

[2]TU Dortmund University, Dortmund, Germany

[3]Norwegian Defence Research Establishment, Oslo, Norway

Corresponding author: Joseph Henry LaCasce, j.h.lacasce@geo.uio.no

(Received 18 November 2025; revised 18 February 2026; accepted 26 March 2026)

The instability of baroclinic Rossby waves over two-dimensional topography is examined using a nonlinear model, a linear stability calculation and wave triads. In all cases, the Rossby waves are unstable, as seen previously over a flat bottom. But topography decreases the growth rates and changes the structure of the unstable waves. When the topographic height (or slope) exceeds a critical value, the instability is 'locked' to topography, in that the most unstable mode, particularly in the lower layer, resembles the bathymetry. In this limit, the growth rate becomes independent of topographic height. A triad calculation suggests that the growth rates in the locked state should depend on the lateral scale of the bathymetry but not its height, and that locking does not occur for topographic scales smaller than the surface deformation radius. The results suggest an alternate way that topographically locked flow can be generated, and indicate that baroclinic instability can be much different over steep bathymetry.

Key words: baroclinic flows, ocean circulation, topographic effects

1. Introduction

Large-scale planetary (Rossby) waves are observed at the low and mid latitudes over much of the world ocean (Kessler 1990; Chelton & Schlax 1996; Zang & Wunsch 1999; Cipollini *et al.* 2001; Osychny & Cornillon 2004; Jury 2018). The waves were first predicted by Rossby (Rossby 1939; Platzman 1968; Madden 1979) and are routinely invoked in atmospheric dynamics, for instance with respect to 'teleconnections' (Ambrizzi, Hoskins & Hsu 1995; Galanti & Tziperman 2003; Rivière 2010; Tseng, Maloney & Barnes 2019). Rossby waves exist because of the beta effect – the meridional gradient of the Coriolis parameter (which increases monotonically with latitude). Because of β,

© The Author(s), 2026. Published by Cambridge University Press. This is an Open Access article, distributed under the terms of the Creative Commons Attribution licence (https://creativecommons.org/licenses/by/4.0/), which permits unrestricted re-use, distribution and reproduction, provided the original article is properly cited.

https://doi.org/10.1017/jfm.2026.11482 Published online by Cambridge University Press

meridional motion alters the vorticity on fluid parcels, and the resulting restoring force supports waves.

In the ocean, Rossby waves are seen clearly in satellite observations of sea surface height. These are primarily 'baroclinic' Rossby waves, which have vertical shear and longer time scales than unsheared 'barotropic' waves. A signature of the baroclinic waves is westward phase propagation, with a phase speed that is largest at the equator and decreasing towards the poles. Such propagation is seen in all major ocean basins, outside boundary currents like the Gulf Stream and the Antarctic Circumpolar Current. In the tropics (20S to 20N), the waves are large, exceeding thousands of kilometres, but they are smaller at higher latitudes, closer to the internal 'deformation scale' (typically tens of kilometres). Furthermore, at mid and high latitudes, the waves are more nonlinear, exhibiting meridional propagation as well; cyclones are deflected to the north-west, and anticyclones to the south-west (Chelton, Schlax & Samelson 2011).

The phase speed at low latitudes is comparable to the theoretical long wave speed for traditional, first baroclinic mode Rossby waves, the gravest of the vertically sheared modes (Chelton & Schlax 1996). However, the speeds outside the 20S–20N range are consistently faster than predicted – in some cases twice as fast. A number of explanations have been proposed, but the most likely is that the waves are modified over a rough bottom (Samelson 1992; Bobrovich & Reznik 1999; Reznik & Tsybaneva 1999; Vanneste 2000; Tailleux & McWilliams 2001; LaCasce 2017; Clarke & Buchanan 2024; Davis *et al.* 2025). Over steep topography, the baroclinic modes have nearly zero flow at the bottom and a larger deformation radius; as the long wave phase speed is proportional to the deformation radius squared, the waves are faster (LaCasce & Groeskamp 2020). Current meter observations suggest that such 'rough bottom modes' are common in the ocean (de La Lama *et al.* 2016).

Less attention has been paid to the change in the lateral scale of the waves, from large structures at low latitudes to deformation scale, vortex-like features at higher latitudes. One proposed explanation is that a turbulent inverse energy cascade transitions to Rossby waves at different scales, due to the latitudinal variation of β (Theiss 2004). Another explanation is that the Rossby waves are unstable. This instability has been explored in the barotropic context (Lorenz 1972; Gill 1974) and the baroclinic one (Jones 1978, 1979; Vanneste 1995; LaCasce & Pedlosky 2004). Originating at the eastern boundary, the wave crests are oriented approximately north–south, and as such, shear instability cannot be stabilised by β (Kamenkovich & Pedlosky 1996).

The question then is how far the waves propagate into the interior before breaking into smaller eddies. At low latitudes, the waves move faster and cross the basin intact, but the slower waves at higher latitudes succumb before crossing. The difference can be quantified by a parameter Z defined by

$$Z = \frac{T_c}{T_g} = \frac{U L_b}{\beta L_{d1}^3}\,, \tag{1.1}$$

i.e. the ratio of the crossing time to the unstable growth time (LaCasce & Pedlosky (2004), LP04 hereafter). Here, L_b is the basin scale, and L_{d1} is the first baroclinic deformation radius, while β is the meridional gradient of the Coriolis parameter (f), and U is a velocity scale. As the deformation radius is inversely proportional to f, Z increases rapidly with latitude. It is near unity at 20°, in line with observations that smaller scale eddies dominate outside the range 20S–20N. LP04 employed quasi-geostrophic (QG) dynamics, but consistent results are obtained under the full primitive equations (Isachsen, LaCasce & Pedlosky 2007).

https://doi.org/10.1017/jfm.2026.11482 Published online by Cambridge University Press

However, these previous studies were conducted with a flat bottom. The results could well vary with bottom roughness, which affects baroclinic instability (De Szoeke 1983; Benilov 2001; Vanneste 2003; LaCasce *et al.* 2019; Radko 2019; Davies, Khatri & Berloff 2021; Palóczy & LaCasce 2022). One-dimensional ridges are particularly effective in this regard, suppressing deep motion perpendicular to the ridges, but suppression occurs as well with two-dimensional relief. Topography impacts the growth rates and scales of the resulting eddies, and in turbulent flows can scatter energy to both smaller and larger scales (Rhines 1977; Owens & Bretherton 1978; Treguier & Hua 1988; Treguier & McWilliams 1990; Palóczy & LaCasce 2022; Zhang & Xie 2024; Pudig & Smith 2025).

Hereafter, we examine how two-dimensional relief affects Rossby wave stability and characteristics. Rossby waves have lateral shear and are time dependent, so we employ simplified dynamics (two fluid layers, the QG approximation and sinusoidal bathymetry). As will be seen, topography does not inhibit the instability of large waves, so the predicted latitudinal dependence should be unaltered from LP04. But if the topographic height exceeds a critical value, then the unstable growth is essentially locked to the bathymetry. Then the growth rate is independent of topographic height, and the horizontal scale of the resultant eddies is determined by topography. As such, the instability is significantly different over a flat bottom.

The equations are presented in § 2. Nonlinear simulations in a basin, similar to those by LP04, are discussed in § 3, and the linear stability calculations in § 4. In § 5, the presented theory is applied to Earth's oceans. The results are summarised and discussed thereafter.

2. The QG equations

We employ the two-layer QG potential vorticity (PV) equations. The QG approximation, which assumes hydrostatic balance and a small Rossby number, is reasonable for synoptic-scale oceanic applications (Pedlosky 1979; Vallis 2017). The unknowns are the geostrophic streamfunctions in the upper and lower layers, ψ_1 and ψ_2. These are related to the PV in the corresponding layers via

$$q_i = \nabla^2\psi_i + F_i\,(\psi_{3-i} - \psi_i)\,, \tag{2.1}$$

where $F_i = L^2/L_{di}^2 = f_0^2L^2/(g'H_i)$ are inverse Burgers numbers. Here, f_0 is the mean Coriolis parameter, $g' = (\rho_2 - \rho_1)g/\rho_c$ is the reduced gravity (where ρ_c is the mean of the layer densities), and H_i is the depth of the ith layer at rest. The parameter L is the domain scale, such that the model basin has dimensions $\pi \times \pi$.

In the absence of external forcing or damping, the PV evolves following (Pedlosky 1979; Vallis 2017)

$$\frac{\partial q_1}{\partial t} + J(\psi_1, q_1) + \beta\frac{\partial \psi_1}{\partial x} = D_1, \tag{2.2}$$

$$\frac{\partial q_2}{\partial t} + J(\psi_2, q_2) + \beta\frac{\partial \psi_2}{\partial x} + J(\psi_2, h) = D_2, \tag{2.3}$$

where $J(\cdot,\cdot)$ is the Jacobian operator, and the D_i represent small-scale dissipation. There are two parameters that determine the response. The first is the (scaled) meridional gradient of the Coriolis parameter:

$$\beta \equiv \frac{\beta_d L^2}{U}, \tag{2.4}$$

https://doi.org/10.1017/jfm.2026.11482 Published online by Cambridge University Press

where β_d is the dimensional gradient, and U is the velocity scale of the wave. With a large β, the dynamics are wave-like to first order, as in the small-Z limit of LP04 (1.1).

The other parameter is the non-dimensional topographic height:

$$h \equiv \frac{f_0 L h_d}{U H} = \frac{1}{R_o}\frac{h_d}{H}. \tag{2.5}$$

Here, $R_o = U/(f_0 L)$ is the Rossby number based on the domain scale, and $H = H_1 + H_2$ is the total depth. We have assumed that the topography has a scale comparable to that of the domain; this is relaxed later. If the latter is 1000 km, then $R_o \approx 10^{-3}$. If the depth is of order 1000 m, as in the ocean interior, the non-dimensional topographic height translates approximately to metres: $h = 1$ indicates dimensional height $h_d \approx 1$ m.

Hereafter, we fix the layer depth ratio at 1/4:

$$\delta \equiv \frac{\delta_1}{\delta_2} = \frac{H_1/H}{H_2/H} = \frac{1}{4}. \tag{2.6}$$

This mimics the density stratification in the ocean interior. For the inverse Burgers number, a value $F_1 = 500$ implies that the basin size is 22.4 times the surface deformation radius. The latter is of order 30–40 km at mid latitudes (LaCasce & Groeskamp 2020).

Under the PV equations, the total energy, the sum of the layer kinetic energies and the potential energy, is conserved in the absence of dissipation. The constituents are defined as

$$KE_i = \frac{\delta_i}{2}\iint |\nabla\psi_i|^2 \,\mathrm{d}A, \quad PE = F\iint |\psi_1 - \psi_2|^2 \,\mathrm{d}A. \tag{2.7}$$

The pre-factor of the potential energy is $F = \delta_1 F_1 = \delta_2 F_2$.

We employ two numerical models. The first is a nonlinear, two-layer basin code with topography; the second is a numerical linear stability routine. We present the models and the corresponding results in the respective sections.

3. Semi-spectral model

3.1. *Model and initial condition*

The nonlinear model solves (2.2)–(2.3) in a bounded square domain using finite differences (LaCasce 2002; LaCasce & Pedlosky 2004; Brændshøi 2018). The model has a rigid upper surface and permits variable bottom relief. The model employs third-order Adams–Bashforth time stepping, and the PV (2.1) is inverted for the streamfunctions using sine transforms. The advective (Jacobian) terms are calculated using the third-order QUICK scheme of Leonard (1979). This method introduces implicit (hyperdiffusive) dissipation that preferentially damps the small scales (e.g. Becker & Salmon 1997). The effective diffusivity is proportional to the flow speed and is a sensitive function of the grid spacing (to the third power). While convenient in some respects, for instance with regards to flow parallel to the walls, it does result in a degree of eddy damping, as seen hereafter.

The model is formulated in terms of barotropic and baroclinic modes defined by

$$\psi_B = \delta_1\psi_1 + \delta_2\psi_2, \quad \psi_T = \psi_1 - \psi_2, \tag{3.1}$$

respectively. This facilitates the PV inversions. All runs with this model use 512×512 resolution.

A significant issue is the boundary condition for the baroclinic streamfunction ψ_T. Both streamfunctions are constant along the walls, to ensure no-normal flow. For the barotropic mode, this constant can be assumed to be zero, due to the rigid lid, but the baroclinic streamfunction is non-zero and can vary in time (Flierl 1977; McWilliams 1977; LaCasce

https://doi.org/10.1017/jfm.2026.11482 Published online by Cambridge University Press

2000). Thus we introduce an additional variable $\Gamma(t)$, the value of ψ_T on the boundary; this is determined at each time step by imposing conservation of mass. Allowing Γ to vary in time is equivalent to letting the layer interface move up and down on the boundaries. This is the model's representation of Kelvin waves, which are infinitely fast under the QG approximation.

For the initial condition, we assume a surface-trapped Rossby wave:

$$\psi_1 = \sin(k_w x)\sin(y), \quad \psi_2 = 0, \tag{3.2}$$

where the wavenumber is $k_w = n\pi/L_x$, to ensure an integral number of wavelengths in the domain. Note that the initial wave differs from that of LP04, which was purely baroclinic. As noted, a surface wave is more consistent with observations (de La Lama *et al.* 2016). Using a surface wave also avoids a direct interaction with the bathymetry initially (although a surface-trapped wave will generate flow in the lower layer because of interfacial motion, as seen below). In many of the simulations, we fix $F_1 = 500$, corresponding to a deformation wavenumber $K_{d1} = 22.4$.

We employ two types of bathymetry (e.g. Palóczy & LaCasce 2022). One is a two-dimensional random field with a narrow-band spectrum (e.g. Constantinou 2015; He & Wang 2024; Pudig & Smith 2025). The second is an isotropic, monochromatic function:

$$h = h_0 \cos(k_t x)\cos(l_t y). \tag{3.3}$$

The results with both are consistent, but the topographic influence is more easily discerned when using monochromatic bathymetry. We set $k_t = l_t = p$, with $p = 8$ or 10. As such, the topographic scale exceeds the surface deformation scale, with $K_{d1}/K_t = 1.6{-}2$. We will focus on the response to different amplitudes h_0, and return to the random bathymetry when considering stability.

3.2. *Results*

For context, consider the response with a flat bottom ($h = 0$). An example with $\beta = 0.1$ is shown in figure 1. The small value of β corresponds to a large Z in (1.1), implying that the wave moves little over the time scale for unstable growth (as at mid latitudes). The solution with a larger β is qualitatively similar, except that the waves move across the basin while breaking down.

The wave crests and troughs twist initially under mutual advection (figure 1*a*); this is because the waves have a sinusoidal dependence on y (as opposed to the nearly meridionally invariant profile used by LP04). The waves then break up into deformation scale eddies. These subsequently merge, yielding an inverse energy cascade (figure 1*c*). Vortices are seen as well at late times, but the flow is dominated by two large gyres, anticyclonic in the north, and cyclonic in the south. These 'Fofonoff gyres' (Fofonoff 1955; Marshall & Nurser 1986) are often observed in simulations of two-dimensional turbulence in a basin (Griffa & Salmon 1989; Cummins 1992; Wang & Vallis 1994; LaCasce 2002). The lower-layer streamfunctions (not shown) are very similar to those in the upper layer, as expected for barotropic flow. Indeed, there is a significant vertical transfer of energy (as the initial condition is surface-trapped).

The essential elements of the evolution are captured by two-dimensional wavenumber spectra for the layer kinetic energies, shown in the lower panels of figure 1 for the surface energy. Here,

$$\widehat{KE}_1(k,l) = \frac{\delta_1}{2} K^2 |\hat{\psi}_1|^2, \tag{3.4}$$

https://doi.org/10.1017/jfm.2026.11482 Published online by Cambridge University Press

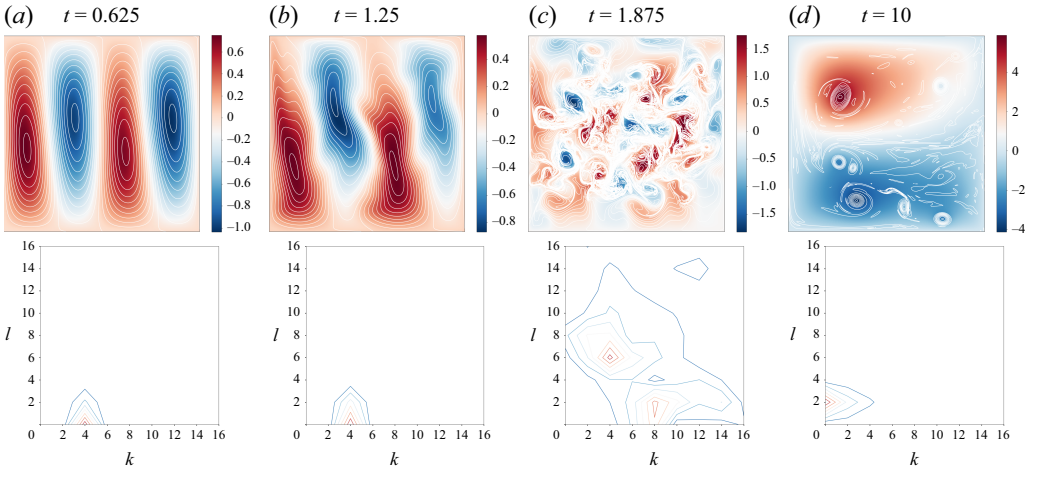


Figure 1. Flat bottom results for $F_1 = 500$ and $\beta = 0.1$. Upper row: the colour fields are the surface streamfunction ψ_1, while the white contours are the surface PV, q_1. Bottom row: the upper-layer two-dimensional kinetic energy spectra at the same times.

where the hat indicates the Fourier transform, and $K = \sqrt{k^2 + l^2}$ is the magnitude of the horizontal wavenumber. Initially, the spectrum reflects the wave, with $k = k_w = 4$ and $l \approx 0$. By $t = 1.875$, the spectrum is more isotropic (figure 1*c*), due to the baroclinic eddies. The dominant wavenumber is $K \approx 8$, somewhat less than $\sqrt{F} = \sqrt{\delta_1 F_1} = 10$. Eventually, the energy is concentrated near $(k, l) \approx (0, 2)$, reflecting the Fofonoff gyres. The plots for $\widehat{KE}_2(k, l)$ are similar, as the late-time flow is nearly barotropic.

This evolution is as described by LP04, allowing for minor differences due to the choice of initial wave. With small-amplitude topography ($h < 1$), the evolution is similar to that with a flat bottom. The primary difference is that the energy at late times, still predominantly near $k = 0$, is spread over more meridional wavenumbers (not shown). This is due to topographic perturbations of the Fofonoff gyres.

With larger heights, topographic effects are more pronounced. The case with $h = 10$ (i.e. 10 m bumps) is shown in figure 2. Instability proceeds initially as in the flat bottom case (figure 2*a*), with the primary wave becoming unstable and generating smaller-scale eddies. Indeed, the topographic influence is not obvious in the streamfunctions (upper panels of figures 2*b*,*c*), but it is seen in the spectra, with a peak at $(k, l) = (10, 10)$, the topographic wavenumbers. Nevertheless, the large-scale wave is still evident in animations, propagating westwards (not shown), and the system eventually evolves to Fofonoff gyres (figure 2*d*). But the streamfunction reveals the topography as well, and both gyres and topographic-scale eddies are present. As before, the lower-layer streamfunction is similar since the baroclinic eddies are strongly barotropic.

An example with higher topography ($h = 100$) is shown in figure 3. Note that the corresponding dimensional value is approximately 100 m in the ocean interior, which is less than 10 % of the total water depth, in line with the QG approximation. Compared to the $h = 10$ case, wave instability proceeds more slowly; compare figures 3(*b*,*c*) with figures 2(*b*,*c*). Eventually, the wave does break up, but the Fofonoff gyres are absent at late stages (figure 3*d*). Rather, the flow is locked to the bathymetry. The spectra confirm this, with a single peak at $(k, l) = (10, 10)$. The final state is thus very different to that over a flat bottom.

https://doi.org/10.1017/jfm.2026.11482 Published online by Cambridge University Press

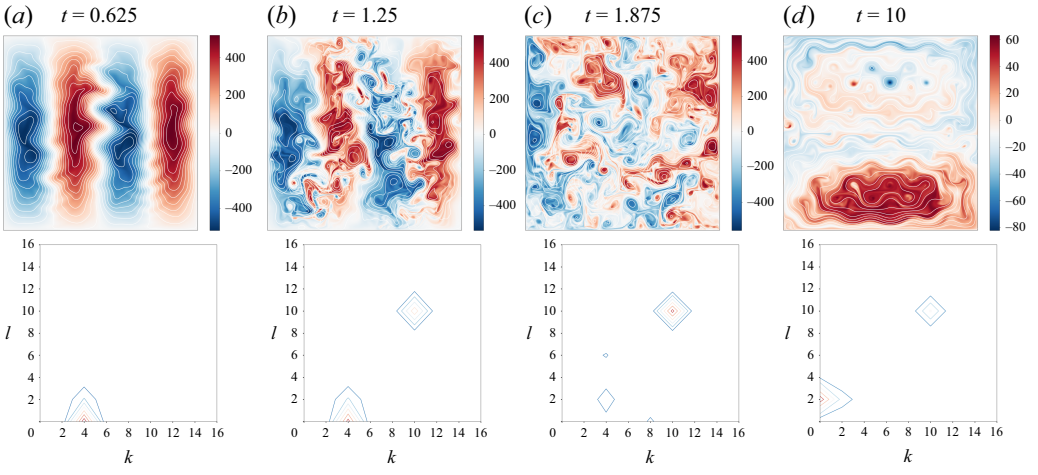


Figure 2. As in figure 1 but with moderate-amplitude topography ($h_0 = 10$).

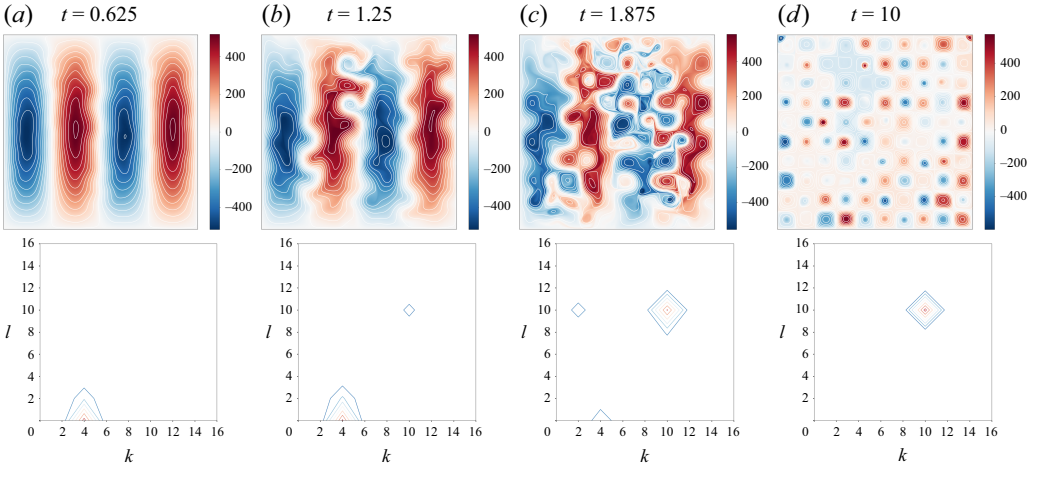


Figure 3. As in figure 1 but with large-amplitude topography ($h_0 = 100$).

Despite the differences, the energetics evolve similarly in the three cases (figure 4). This is due primarily to the large value of F_1, which ensures that the base wave's potential energy is large. But topography induces secondary changes. With moderate bathymetry ($h = 10$), instability occurs earlier than over a flat bottom. In fact, the growth rate is actually smaller in the former case, but the topography evidently perturbs the base wave (most likely because interfacial motion drives flow in the lower layer). Higher bathymetry suppresses the growth rate further, consistent with previous studies (Benilov 2001; Vanneste 2003; LaCasce *et al.* 2019; Radko 2019; Davies *et al.* 2021; Palóczy & LaCasce 2022). But with so much potential energy, instability proceeds regardless.

Note that the total energy in the runs (figure 4*b*) decreases in all cases, indicating that energy is not conserved. In the simulated time period, the decrease is up to 20 %, depending on the topographic height. The loss occurs because the baroclinic eddies, much smaller than the primary wave, are more susceptible to the implicit numerical dissipation associated with the advective scheme (§ 3.1). The effect is more pronounced with random

https://doi.org/10.1017/jfm.2026.11482 Published online by Cambridge University Press

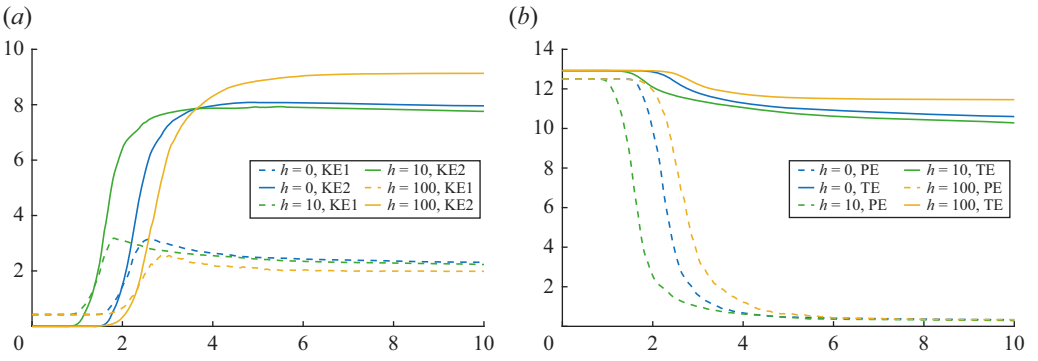


Figure 4. Energy terms for runs with $h = 0$, 10, 100: (a) kinetic energies and (b) potential (PE) and total (TE) energies.

topography, as energy is scattered to still smaller scales, as discussed hereafter. Running at higher resolution or with a larger deformation radius reduces the loss.

To summarise, Rossby wave instability proceeds largely as over a flat bottom with small topographic heights ($h < 1$). With large β, the waves propagate across the basin before disintegrating, and with small β, they are nearly stationary as they break up. In both cases, the flow eventually becomes turbulent, and an inverse cascade yields Fofonoff gyres. With $h > 10$, the topography dominates both the instability and the subsequent turbulent evolution. There are indications that the instability involves multiple wavenumbers, but the energy quickly settles at the topographic wavenumbers.

Why does the flow become locked to the bathymetry? Topographically locked flows can result from turbulent cascades in two dimensions (Bretherton & Haidvogel 1976; Salmon, Holloway & Hendershott 1976; Carnevale & Frederiksen 1987*a*; Siegelman & Young 2023; LaCasce, Palóczy & Trodahl 2024). But topography apparently alters the instability itself in these simulations, favouring energy transfer directly to the topographic scales. This is considered next.

4. Linear stability

Linear stability over rough topography has been studied analytically using multi-scale expansions (Benilov 2001; Vanneste 2003; Radko 2019). However, using topography with scales comparable to those of the base flow generally requires a numerical approach (LaCasce *et al.* 2019; Davies *et al.* 2021; Palóczy & LaCasce 2022), as employed hereafter. Following the previous results, we focus on the small β (mid latitude) case, in which instability proceeds on a time scale that is short compared to the wave period.

4.1. *Model*

Following LP04, we introduce two time scales in the QG PV (2.2)–(2.3), one for wave propagation, and one for unstable growth:

$$T = \beta^{-1} t, \quad t_g = t. \tag{4.1}$$

With these, the equations become

$$\frac{\partial q_1}{\partial t} + \beta \frac{\partial}{\partial T} q_1 + J(\psi_1, q_1) + \beta \frac{\partial \psi_1}{\partial x} = 0, \tag{4.2}$$

$$\frac{\partial q_2}{\partial t} + \beta \frac{\partial}{\partial T} q_2 + J(\psi_2, q_2) + \beta \frac{\partial \psi_2}{\partial x} + J(\psi_2, h) = 0 \tag{4.3}$$

https://doi.org/10.1017/jfm.2026.11482 Published online by Cambridge University Press

(after dropping the small-scale dissipation terms). The β terms dominate at low latitudes, and the other terms dominate elsewhere. The instability is qualitatively similar in both cases, so we focus hereafter on the small-β limit and ignore those terms.

We linearise the equations about the wave:

$$\psi_1 = \Psi_1 + \psi_1', \quad q_1 = Q_1 + q_1', \tag{4.4}$$

$$\psi_2 = \psi_2', \quad q_2 = Q_2 + q_2', \tag{4.5}$$

where

$$Q_1 = -(k_w^2 + F_1)\Psi_1, \quad Q_2 = F_2\Psi_1. \tag{4.6}$$

As we ignore the β terms, the wave is stationary. Inserting these into the PV equations and neglecting terms with products of primed terms yields

$$\frac{\partial q_1}{\partial t} + \frac{\partial \Psi_1}{\partial x}\frac{\partial q_1}{\partial y} - \frac{\partial Q_1}{\partial x}\frac{\partial \psi_1}{\partial y} = 0, \tag{4.7}$$

$$\frac{\partial q_2}{\partial t} - \frac{\partial \psi_2}{\partial y}\frac{\partial Q_2}{\partial x} + J(\psi_2, h) = 0, \tag{4.8}$$

after dropping the primes. We also neglect the y-variation of the base wave, and assume the following form:

$$\Psi_1 = A\cos(k_w x), \quad \Psi_2 = 0. \tag{4.9}$$

In the cases shown below, we take $k_w = 4$, as in the numerical experiments in the preceding section. Then the linear system reduces to

$$\frac{\partial q_1}{\partial t} + V_w \cos(k_w x)\left[\frac{\partial q_1}{\partial y} + (k_w^2 + F_1)\frac{\partial \psi_1}{\partial y}\right] = 0, \tag{4.10}$$

$$\frac{\partial q_2}{\partial t} - F_2 V_w \cos(k_w x)\frac{\partial \psi_2}{\partial y} + J(\psi_2, h) = 0, \tag{4.11}$$

where $V_w = Ak_w$ is the velocity amplitude of the wave.

The equations are advanced in time using a fourth-order Runge–Kutta method, and the PV is inverted using fast Fourier transforms (Palóczy & LaCasce 2022). When the total perturbation energy reaches a selected value, the streamfunctions are rescaled to 10 % of their value, and the computation proceeds. This is the 'power method' (see https://en.wikipedia.org/wiki/Power_iteration and Constantinou 2015). Typically, three such cycles suffice to obtain the fastest growing wave; we use five hereafter. The calculation yields the spatial structure, growth rate and phase speed of the fastest growing mode.

We examine both monoscale and random topography. We begin with the former, as in (3.3). The topographic wavenumber is here taken to be $p = 8$, so that the topographic scale is larger than the surface deformation radius. The role of smaller-scale features is discussed afterwards. The primary focus again is on varying the topographic height h_0.

4.2. *Results*

Shown in figure 5 are the streamfunctions for the fastest growing mode and the corresponding kinetic energy spectra with $F_1 = 500$, for increasing topographic heights. With a flat bottom ($h = 0$, figure 5*a*), the most unstable wave has lines of deformed eddies in both layers. The eddies are centred along the four regions of maximum meridional velocity, with alternating directions. The eddies exhibit a bowed shape, indicating convergent momentum fluxes; this is because the alternating jets are broader than deformation scale (Held 1975; Flierl, Malanotte-Rizzoli & Zabusky 1987; LaCasce

https://doi.org/10.1017/jfm.2026.11482 Published online by Cambridge University Press

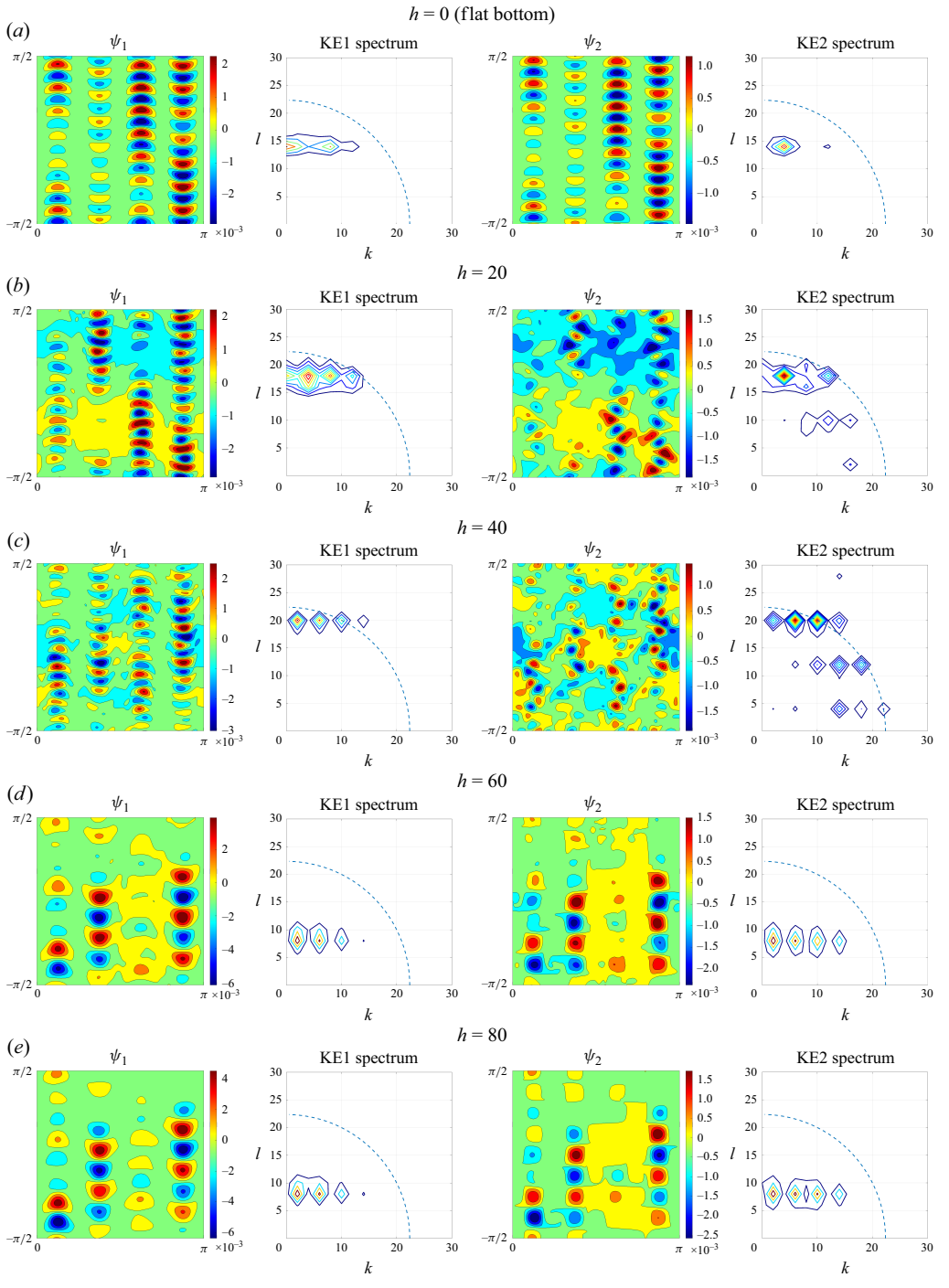


Figure 5. Fastest growing mode in linear stability calculations for $F_1 = 500$. Left to right: ψ_1, KE_1 spectrum, ψ_2, KE_2 spectrum. Top to bottom: increasing topographic height.

https://doi.org/10.1017/jfm.2026.11482 Published online by Cambridge University Press

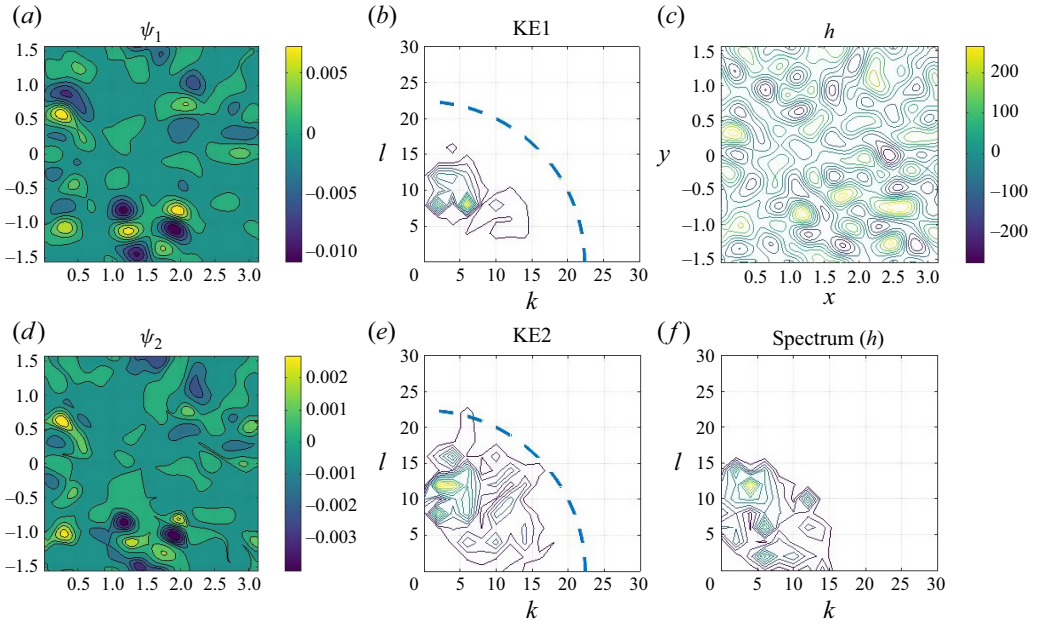


Figure 6. A case with random topography, as shown in (*c*). The amplitude is $h = 100$. The streamfunctions of the most unstable mode are shown in (*a,d*), and the kinetic energy spectra in (*b,e*). The spectrum of the bathymetry is in (*f*).

et al. 2019; Palóczy & LaCasce 2022). The eddies are also tilted in the vertical, in the sense that they 'lean' against the mean flows (Pedlosky 1979; Vallis 2017). Both aspects are typical of jet instability.

The wavenumber spectra (second and fourth columns of figure 5) exhibit peaks with a meridional wavenumber near $l = 15$, somewhat less than the surface deformation wavenumber $\sqrt{F_1} = 22.4$. The peaks for the surface kinetic energy occupy a range of zonal wavenumbers in the upper layer, from 0 to 10, so that the unstable mode is not a single harmonic. The KE_2 spectrum peaks at approximately $k = 4$, the wavenumber of the base wave.

Increasing the topographic height to $h = 20$ yields smaller-scale structures (figure 5*b*). In the upper layer, the eddies are again aligned with the wave's velocity maxima, but are less symmetric than before. The dominant meridional wavenumber has increased to a value near $l = 20$. The structure differs in the lower layer, with a more random orientation, and the spectra reveal a range of scales, with peaks near $l = 2$, 10 and 18. Note that these are separated by the topographic wavenumber 8. Increasing the amplitude further to $h = 40$ yields similar results, with still smaller eddies in both layers (figure 5*c*). Again, the dominant meridional wavenumbers, 4, 12 and 20, are separated by the topographic wavenumber.

When $h > 50$, the response changes drastically. With $h = 60$ (figure 5*d*), the peak meridional wavenumber collapses to $l = 8$, the wavenumber of the topography. The eddies are nearly circular and more closely aligned with the bathymetry. The vertical tilt persists, however, with the upper-layer eddies displaced against the mean shear, as before. The dominant zonal scales are nevertheless spread out, with peaks near $k = 3$, 7 and 10. Thus the base wave still impacts the zonal structure. The response is nearly identical with $h = 80$ (figure 5*e*), and with steeper topography as well (not shown).

The response over random relief is similar. As the topographic height increases, the unstable flow becomes locked to the bathymetry. An example is shown in figure 6.

https://doi.org/10.1017/jfm.2026.11482 Published online by Cambridge University Press

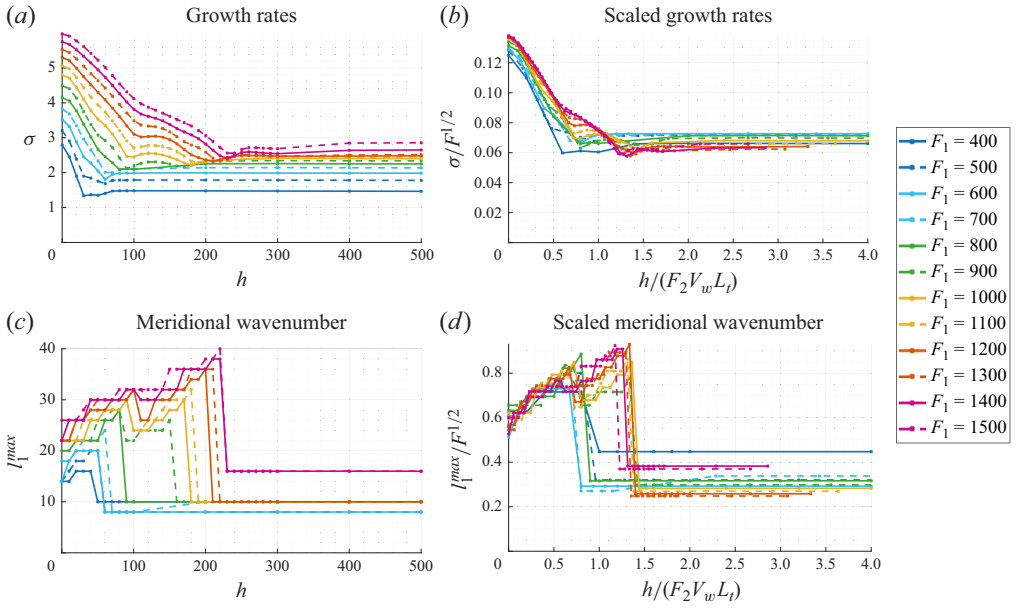


Figure 7. Instability growth rates and dominant meridional wavenumbers in the upper layer for a suite of runs.

The topography is plotted in figure 6(*c*), with the wavenumber spectrum shown in figure 6(*f*). The chosen function has contributions over wavenumbers 5–15, with random phases (e.g. Constantinou & Young 2017; He & Wang 2024; Pudig & Smith 2025), and the amplitude is $h = 100$. The kinetic energy spectra exhibit peaks in the same range as the bathymetry and are similarly isotropic. The locking is clear when superimposing plots of ψ_2 and $h(x, y)$ (not shown). However, ψ_2 exhibits peaks in only a few of the same locations; this is because eddy formation is strongest beneath the velocity maxima of the waves, as noted before. As such, the topographic influence is harder to distinguish in this case.

The response also depends strongly on the Burgers number. This is seen when comparing growth rates for the most unstable mode (figure 7). The largest growth rates are obtained with a flat bottom, and larger values of F_1 yield faster growth (figure 7*a*). The growth rates decrease with increasing topographic height, in line with topographic suppression of baroclinic instability. However, beyond a certain amplitude, the growth rates are constant. Thus there is actually a limit to the topographic suppression of instability. The transition to the fixed growth rate varies with F_1, and occurs with larger heights when F_1 is larger. With $F_1 = 500$, the required height is approximately $h = 50$, but it is larger ($h = 200$) with $F_1 = 1500$.

The meridional scale of the fastest growing mode also varies with the topographic height (figure 7*c*). The meridional wavenumber grows as h increases from zero, but when h is larger than a critical height, the meridional wavenumbers collapse to a value near 8, the wavenumber of the topography. This is true with different values of F_1, although the transition occurs again at different heights. In the cases with the largest F_1, the final meridional wavenumber is somewhat larger than that of the topography, closer to $l = 16$.

4.3. *Scalings and transition topographic height*

The curves in figure 7 can be collapsed, approximately, following appropriate scaling. Both the growth rate and the meridional scale of the most unstable mode scale as $F^{1/2}$ over a

https://doi.org/10.1017/jfm.2026.11482 Published online by Cambridge University Press

flat bottom (LP04). This accounts for the increase in both quantities with $h = 0$ seen in figures 7(*a*) and 7(*c*). The topographic height scaling, on the other hand, follows from the ratio of the third and second terms in (4.11):

$$\frac{h}{F_2 V_w L_t} \equiv \frac{h}{h_c}, \tag{4.12}$$

where again V_w is the wave meridional velocity, and L_t is the topographic scale. Note that we allow the latter to vary, rather than assuming that it is equivalent to the basin scale as in § 2. This defines a critical height

$$h_c = F_2 V_w L_t. \tag{4.13}$$

If $h \ll h_c$, then the lower-layer PV equation is dominated by the stretching term, as over a flat bottom, but if $h \gg h_c$, then the topographic term dominates. The ratio h/h_c is the inverse of the Λ parameter of LaCasce (1998), and a similar critical height, h_c, was proposed by Pudig & Smith (2025) in the context of baroclinic turbulence over topography. The latter observed a similar transition to topographically locked flow when $h > h_c$.

Rescaling the growth rates and the most unstable wavenumbers using these factors yields the curves in figures 7(*b*,*d*). The growth rates collapse fairly well onto a single curve, with the scaled growth rates nearly constant above $h = h_c$. The implied growth rate is

$$\sigma \approx 0.065 F^{1/2} \tag{4.14}$$

in most of the simulations. The collapse is less clean with the meridional wavenumber. As noted, the final meridional wavenumber is somewhat higher with a larger F, and the change in the scaled growth rate is non-monotonic with F. This suggests that topography has an additional effect on the growth rates not captured by the $F^{1/2}$ scaling. But a transition near $h_c = 1$ is evident nevertheless.

Interestingly, topographic locking does not occur for smaller values of F_1, even with large topographic amplitudes. This is seen in a case with $F_1 = 200$ (figure 8). In figures 8(*a*,*e*), the topographic wavenumbers are $(k, l) = (10, 10)$, and the height $h = 50$ corresponds to scaled height approximately $4h_c$. Despite this, there is little indication of energy at the topographic wavenumber; rather, the response is like that with the intermediate topographic heights with $F_1 = 500$, with asymmetrically bent eddies and a meridional scale smaller than that of the topography ($l = 20$). However, with wider bumps ($(k, l) = (4, 4)$), the unstable wave is again locked to the topography, particularly in the lower layer.

4.4. *Triad exchanges*

Thus there are at least two curious aspects from the stability calculations: the lack of topographic locking with small F_1, and the constant growth rates when $h > h_c$. The latter in particular is unexpected, given previous work on instability over roughness (Benilov 2001; Vanneste 2003; LaCasce *et al.* 2019; Davies *et al.* 2021). To understand both, we consider energy exchanges among triads of waves (Salmon 1978, 1980; Fu & Flierl 1980). Triads have been used previously for studying wave stability (Gill 1974; Jones 1978; Vanneste 1995; LaCasce & Pedlosky 2004). An advantage of a triad calculation is that no assumption about the horizontal scale of the bathymetry is necessary.

The equations permit two triads. The first, the 'wave triad' hereafter, consists of

$$\Psi_{w1} = A\cos(k_w x), \quad \Psi_{2w} = 0, \tag{4.15}$$

$$\psi_{t1} = b(t)\cos(kx)\cos(ly), \quad \psi_{t2} = c(t)\cos(kx)\cos(ly), \tag{4.16}$$

$$\psi_{c1} = d(t)\sin(mx)\sin(ny), \quad \psi_{c2} = e(t)\sin(mx)\sin(ny). \tag{4.17}$$

https://doi.org/10.1017/jfm.2026.11482 Published online by Cambridge University Press

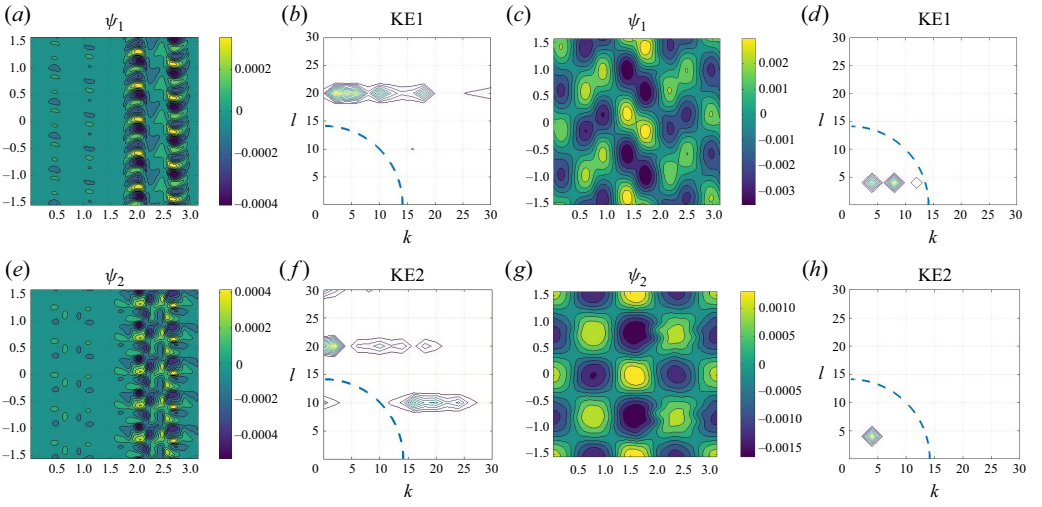


Figure 8. The fastest growing modes with $F_1 = 200$ and $h = 50$. In (a,e), the topographic wavenumbers are $(k, l) = (10, 10)$, and in (c,g), $(k, l) = (4, 4)$.

The first is the (stationary) Rossby wave, assumed surface-trapped as in the previous sections. The second is a 'test wave' with variable wavenumbers. The third is a catalyst wave whose wavenumbers are determined by the triad conditions, which involve integrals of sinusoids. The wave amplitude A is assumed much larger than amplitudes of the other waves, and is fixed, linearising the resulting equations. The sinusoidal representation above differs somewhat from the observed most unstable mode, which is intensified beneath the wave velocity maxima, but the response is informative nevertheless.

Substituting the waves into the inviscid PV (2.2)–(2.3) and integrating over the domain yields a set of four equations for the amplitudes b, c, d, e. Energy transfer occurs among two classes of triads, one involving the Rossby wave, and a second involving the bathymetry. We assume the latter to also be sinusoidal and given by (3.3), with $k_t = l_t = p$, as in the preceding sections.

The wavenumbers in the first triad class obey

$$m = \pm k_w \pm k, \quad n = \pm l. \tag{4.18}$$

The catalyst has the same meridional scale as the test wave, but is shifted by 90° and has a different zonal wavelength. Note too that the topography does not enter; as such, the same triad is obtained over a flat bottom. After rearranging, the equations for the amplitudes can be written as

$$-L_1\dot{b} + F_1\dot{c} = \gamma(K_1 - M_1)d + \gamma F_1 e, \tag{4.19a}$$

$$F_2\dot{b} - L_2\dot{c} = -\gamma F_2 e, \tag{4.19b}$$

$$-M_1\dot{d} + F_1\dot{e} = \gamma(L_1 - K_1)b - \gamma F_1 c, \tag{4.19c}$$

$$F_2\dot{d} - M_2\dot{e} = \gamma F_2 c, \tag{4.19d}$$

where the dot indicates a time derivative, and the parameters are given by

$$K_1 = k_w^2 + F_1, \quad L_i = k^2 + l^2 + F_i, \tag{4.20}$$

$$M_i = m^2 + n^2 + F_i, \quad \gamma = \frac{k_w l A}{2}. \tag{4.21}$$

https://doi.org/10.1017/jfm.2026.11482 Published online by Cambridge University Press

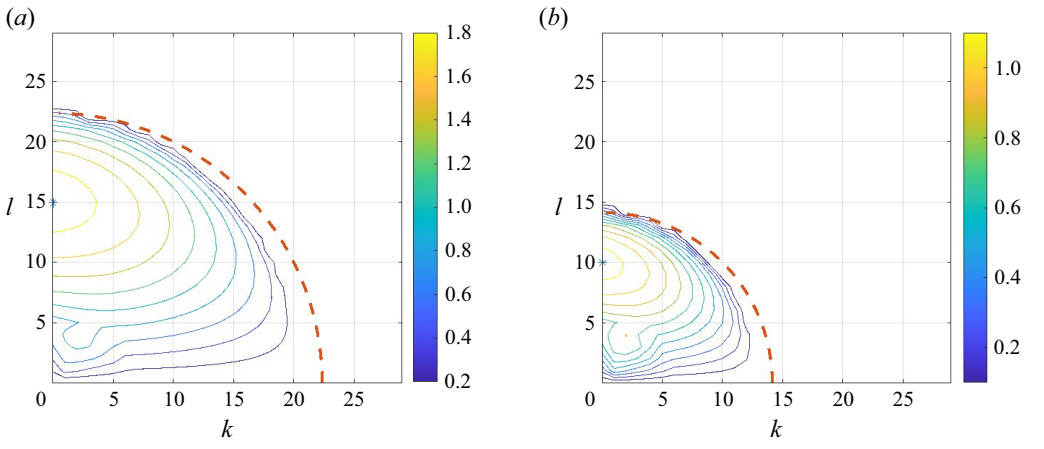


Figure 9. Growth rates for wave triads with (*a*) $F_1 = 500$ and (*b*) $F_1 = 200$. The mode with the maximum growth is indicated by the asterisks. The dashed curves represent the surface deformation wavenumber, such that $k^2 + l^2 = F_1$.

Assuming exponential growth with rate σ, the system can be solved as a generalised eigenvalue problem. The eigenvalues are usually two sets of conjugate pairs, with one set growing in time, and the other decaying.

The growth rates from the primary triads are plotted in figure 9, for two values of F_1. With $F_1 = 500$, the fastest growth is for a test wave with wavenumbers $(k, l) = (0, 15)$ (as indicated by the asterisk). This is consistent with the result of LP04, where the most unstable wave was of long zonal extent, perpendicular to the base wave. The meridional wavenumber is close to that of the most unstable wave ($l = 14$) in the numerical linear calculation with $h = 0$ (figure 5*a*). The triad growth rate is roughly half as large (figure 7), most likely due to the aforementioned difference in horizontal structure with the observed most unstable wave.

Significantly, the triad growth rates exhibit a short-wave cut-off, as large wavenumbers have zero growth rates. This applies to wavenumbers with approximately $(k^2 + l^2) > F_1$, indicated by the dashed contour in figure 9(*a*). Thus test waves smaller than the surface deformation radius are stable.

With $F_1 = 200$, the growth rates are reduced, and the most unstable wavenumber shifts to $(k, l) = (0, 10)$ (figure 9*b*). There is again a short-wave cut-off, with waves smaller than the surface deformation radius exhibiting zero growth.

The second triad involves the topography. The wavenumbers of the catalyst wave in this case are given by

$$m = k \pm p, \quad n = \pm l \pm p. \tag{4.22}$$

Now the Rossby wave does not appear. After integrating, the resulting equations are

$$-L_1\dot{b} + F_1\dot{c} = 0, \tag{4.23a}$$

$$F_2\dot{b} - L_2\dot{c} = \frac{ph_0e}{4}(m \pm n), \tag{4.23b}$$

$$-M_1\dot{d} + F_1\dot{e} = 0, \tag{4.23c}$$

$$F_2\dot{d} - M_2\dot{e} = \frac{ph_0c}{4}(\pm l - k), \tag{4.23d}$$

https://doi.org/10.1017/jfm.2026.11482 Published online by Cambridge University Press

with the coefficients on the left-hand sides as defined above. The upper-layer equations have no forcing terms on the right-hand sides because the topography only affects the lower layer. These imply that the upper-layer PV is constant for both waves. This is the case for topographic waves in two layers, which have zero PV in the upper layer (LaCasce 1998). Having $q_1 = 0$ yields a relation between the lower- and upper-layer amplitudes:

$$b = \frac{F_1 c}{L_1} = \frac{F_1 c}{k^2 + l^2 + F_1}, \quad d = \frac{F_1 e}{M_1} = \frac{F_1}{k^2 + l^2 + F_1} e. \tag{4.24}$$

These define the vertical structure of the waves. They are bottom-intensified ($b < c$ and $d < e$), but become more barotropic as the wavelength exceeds the surface deformation radius $F_1^{-1/2}$.

The four equations can be reduced to a single second-order equation, with exponential solutions. The growth rate is found to be

$$\sigma = \pm \left[(k + l \pm 2p)(\pm l - k) \frac{M_1 L_1}{(M_1 M_2 - F_2 F_1)(L_1 L_2 - F_1 F_2)} \right]^{1/2} \frac{p h_0}{4}. \tag{4.25}$$

Exponential growth is obtained if the radicand is positive. The ratio involving the M_i and L_i is positive definite, so the sign is determined solely by the wavenumbers. The growth rate is linearly proportional to the topographic amplitude, so that higher features yield more rapid topographic scattering.

In this formulation, the amplitudes of both the catalyst and the test wave grow exponentially in time. However, the topographic triads are not directly forced by the unstable wave; rather, they scatter the energy injected to the test wave. Thus a more appropriate formulation of the topographic triad would be one in which the amplitude of the test wave, say B, is fixed. The other two members would be the topographic catalyst and a wave locked to the bathymetry.

The question then is how rapidly the test wave extracts energy from the base wave compared to how quickly the energy is scattered to the topographic catalysts and the topographic mode. Consider the fastest growing wave with $F_1 = 500$, with $(k, l) = (0, 15)$ and growth rate approximately $\sigma = 1.9$ (figure 9*a*). Assuming topographic wavenumber $p = 8$ (§ 4.1), the maximum growth rate of the topographic triad is $\sigma = 0.12\, h_0$. Thus the two are equal when $h_0 \approx 20$. When the topography is this high, energy is transferred away from the test wave as quickly as it arrives from the base wave. In such cases, energy should increase at the topographic wavenumber during the unstable growth.

Could energy then be transferred directly to the topography? This can be assessed from the wave triad, with a test wave at the topographic wavenumber, i.e. $(k, l) = (p, p)$. With $F_1 = 500$, the topographic total wavenumber $K = \sqrt{2}p$ is less than the deformation wavenumber $\sqrt{F_1}$, so that energy can grow there. The growth rate is less than at the most unstable mode, however, by approximately 40 % (figure 9*a*). In contrast, such growth could not occur with $F_1 = 200$, as $(k, l) = (10, 10)$ lies just beyond the short-wave cut-off.

Furthermore, when energy is transferred directly to the topography, the second triad is inactive because one cannot construct a triad when the test wave has the same wavenumbers as the topography. Then the growth rate will be independent of the topographic amplitude h_0.

Thus the triads capture several aspects of the observed instability. If the topographic height is large enough, then energy transfer should occur directly to the topographic wavenumbers. The predicted critical height $h_0 \approx 20$ is comparable to that seen with the full stability calculation (§ 4.2) ($h_0 \approx 60$). Topographic locking occurs for topographic scales greater than the surface deformation radius, which explains why it happened with

https://doi.org/10.1017/jfm.2026.11482 Published online by Cambridge University Press

$F_1 = 500$ but not with $F_1 = 200$. And the growth rate for the locked instability is less than the maximum over a flat bottom, as seen in figure 7.

The results are also consistent with the topographic scattering seen when the topographic amplitude is insufficient to lock the instability or when the topographic scale was sub-deformation scale. Then energy also appears at the 'topographic catalysts', with wavenumbers separated by the topographic wavenumber, i.e. $l \pm p$. This is as seen in figure 5 with $h_0 = 20$ and 40.

Nevertheless, the triad calculation does not explain all features of the full linear calculation. The primary difference is with the dominant zonal wavenumbers. In the topographically locked cases, multiple zonal wavenumbers are excited, not just the topographic one (figure 5 with $h_0 = 60, 80$). This is likely due to the aforementioned difference between the observed unstable mode and a simple sinusoid, as the former is more like the response expected with a series of alternating, laterally sheared surface jets (e.g. Palóczy & LaCasce 2022). But the tendencies seen with the triads are qualitatively similar.

5. Topographic locking in the ocean

How high must the bathymetry be to lock the instability? In dimensional terms, the critical height is given by

$$h_c \equiv \frac{F_2 H_2 V_w L_t}{f_0} = \frac{f_0 V_w L_t}{g'}, \tag{5.1}$$

using the definition of F_2. The critical height depends on the wave shear, the stratification and the latitude.

Alternatively, we can write this in terms of a critical bottom slope

$$S_c \equiv \frac{h_c}{L_t} = \frac{f_0 V_w}{g'}, \tag{5.2}$$

which removes the dependence on L_t. The critical height formulation is perhaps better when considering a range of topographic scales, while the critical slope works for simple estimates, as follows. Assuming typical values at mid latitudes,

$$f_0 = 10^{-4}\ \mathrm{s}^{-1}, \quad g' = 0.01\ \mathrm{m\ s}^{-1}, \quad V_w = 0.1\ \mathrm{m\ s}^{-1}, \tag{5.3}$$

yields

$$S_c \approx 10^{-3}, \tag{5.4}$$

or topographic grade 0.1 %.

We can map the ratio of the observed slope to the critical slope using bathymetric data and estimates of the surface velocities. The former were obtained from the ETOPO 2022 Global Relief Model by the NOAA National Centers for Environmental Information. The ETOPO data were first coarsened to a target (0.25°) resolution using area averaging, and the slopes calculated by finite differences with respect to latitude and longitude, followed by conversion to physical gradients on the sphere. The slopes are plotted in figure 10(*a*). They exceed 10^{-3} in most regions, except in localised regions such as the eastern Pacific (see also LaCasce 2017).

We lack estimates of the vertical shear V_w, but we can estimate the velocities using the geostrophic surface eddy kinetic energy (EKE) from satellite measurements of sea surface height. These are available from the Copernicus Marine Data Storage. The data cover most of the world's oceans, excluding parts of the Arctic and Southern Oceans. We use the

https://doi.org/10.1017/jfm.2026.11482 Published online by Cambridge University Press

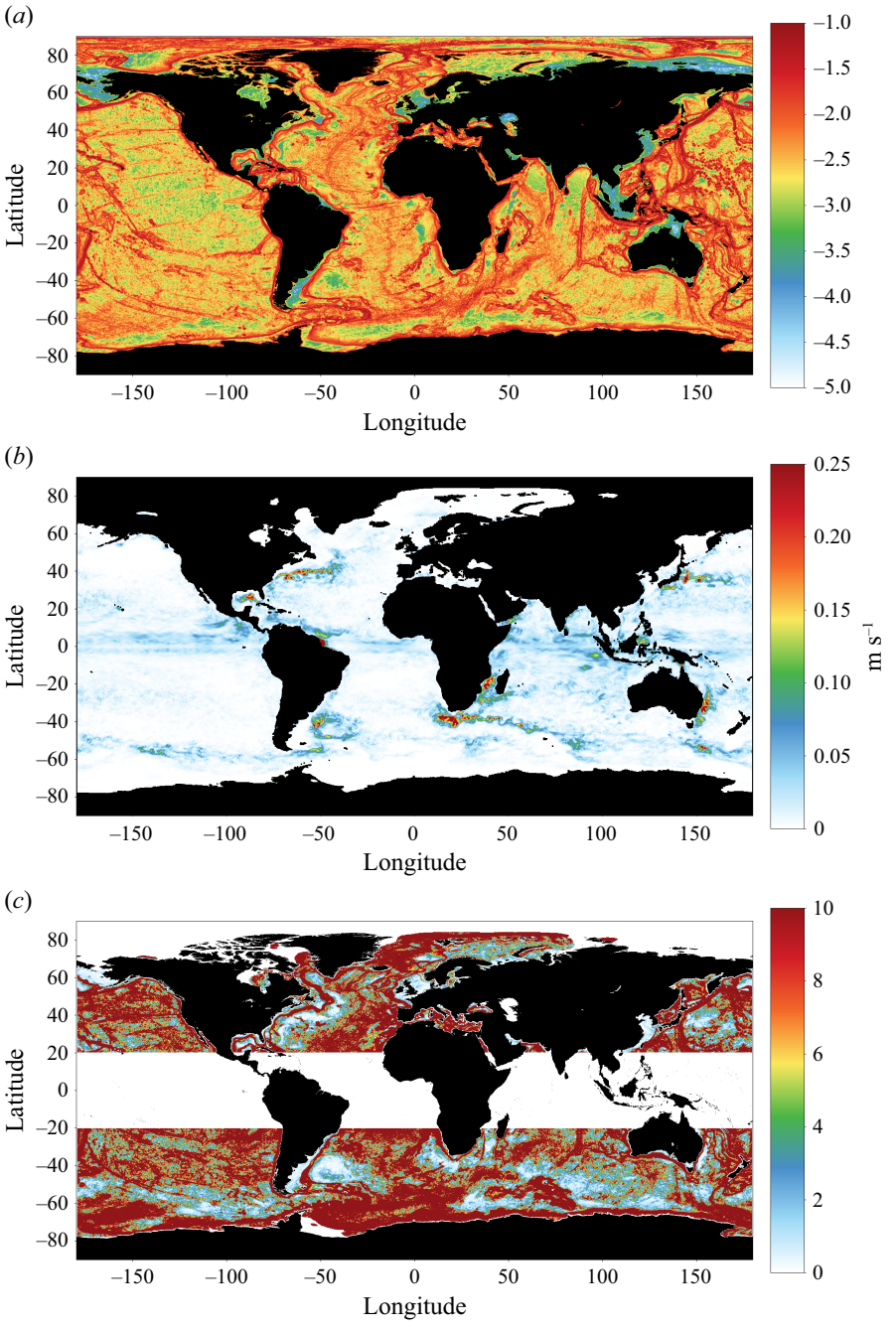


Figure 10. Bathymetric slopes, surface EKE and the ratio of the observed slope to the critical value. (*a*) The topographic slope for 0.25° resolution bathymetry. The data come from the ETOPO 2022 Global Relief Model by the NOAA National Centers for Environmental Information (https://doi.org/10.25921/fd45-gt74). The results are plotted on a $\log_{10}$ scale. (*b*) Surface EKE satellite data from the Copernicus Marine Data Storage (https://doi.org/10.48670/MOI-00149). (*c*) The ratio of the observed slope to the critical value S_c. The values in the latitudes 20S to 20N are excluded as the region is dominated by fast Rossby waves.

https://doi.org/10.1017/jfm.2026.11482 Published online by Cambridge University Press

velocities for a three-month period (January to March 2024), then calculate the variances to obtain the EKE. This is plotted in figure 10(*b*). The largest EKEs occur in the boundary currents (e.g. the Gulf Stream, Kuroshio and Agulhas Currents) and the Antarctic Circumpolar Current (ACC), where root mean square velocities approach $0.5\,\mathrm{m\ s^{-1}}$. The velocities are less in the eastern basins.

In figure 10(*c*), we plot the ratio of observed bathymetric slope to the critical slope. For this, we fix the reduced gravity to $0.01\ \mathrm{m\ s^{-2}}$. The actual values are somewhat greater in the tropics (Zhang & Wu 2010), but this suffices for the present purposes. Also, we exclude the region from 20S to 20N, where Rossby waves cross the basin before succumbing to instability (LP04).

The results suggest that the slope exceeds the critical value nearly everywhere in the extra-tropics. Only in the boundary currents and ACC are the ratios less than 1, because of the large velocities. Current instability dominates in these regions in any case, and free Rossby waves are less likely there. Excluding these regions, the slopes are predominantly supercritical. Thus topographically locked instability could be quite common in the oceans.

6. Discussion

We examined the instability of large-scale Rossby waves over two-dimensional bathymetry. In line with the results of LP04, the waves are always unstable, but topography decreases the growth rates and changes the structure of the most unstable wave. With modest topographic heights, the most unstable waves have smaller meridional scales than over a flat bottom. But when the topographic height (or slope) exceeds a critical value, the meridional scale is set by the topography rather than the deformation radius, and the growth rate becomes independent of topographic height. The resulting unstable mode is thus much different than over a flat bottom.

The results were rationalised using wave triads. There are two types of triad, one involving the base (Rossby) wave, and the second involving the topography. The former applies as well over a flat bottom, while the latter acts to scatter energy from the most unstable wave to the topography and other waves. The fastest growth over a flat bottom occurs for waves with large zonal scales, as found by LP04. The growth rate for topographic scattering is linearly proportional to the topographic amplitude. We reason that if the topographic growth rate exceeds the flat bottom rate, then energy is redirected from the most unstable flat mode directly to the topography, yielding a topographically locked response. Locking occurs only if the lateral scale of the topography exceeds the surface deformation radius, the short-wave cut-off for the flat bottom instability. Then the growth rate, generally less than at the most unstable mode, is independent of the topographic height. Bathymetry with smaller lateral scales instead scatters energy to other scales as well, both smaller and larger, with meridional wavenumbers separated by the topographic wavenumber.

Topographically locked flows are often thought to be driven by eddy fluxes, following seminal works by Bretherton & Haidvogel (1976), Salmon *et al.* (1976) and Carnevale & Frederiksen (1987*b*). In freely evolving turbulent flows, along-isobath flow often develops, with currents parallel to the direction of topographic wave propagation, with shallow water to the right in the northern hemisphere (Solodoch, Stewart & McWilliams 2021; Siegelman & Young 2023; LaCasce *et al.* 2024; Gallet 2024). Topographically-locked oceanic flows have likewise been linked to eddy fluxes (Holloway 2008; Voet *et al.* 2010; Johnston *et al.* 2025). The present results suggest an additional possible explanation for such flows, that they could be generated directly by instability.

https://doi.org/10.1017/jfm.2026.11482 Published online by Cambridge University Press

Using simulations of baroclinic turbulence driven by an imposed baroclinic shear, Pudig & Smith (2025) found that lateral diffusivities exhibit a transition to a value less than that obtained with a flat bottom when the topographic heights exceed the critical value. With larger heights, the diffusivity changes remarkably little. The present results are consistent. In their simulations, energy accumulated at the topographic scales as well, despite the latter being sub-deformation scale. This might reflect nonlinear effects. Indeed, we found clearer topographic locking in the nonlinear solutions (e.g. figure 3) than in the stability solutions. This could, of course, be tested further with a linear model such as that used here.

Using global bathymetric data and satellite-derived EKE, we find that topographic locking may be common nearly everywhere in the extra-tropics. Nevertheless, westward phase propagation at the surface is still observed in most ocean basins, at least to the mid latitudes (Chelton & Schlax 1996; Osychny & Cornillon 2004). Such propagation is expected at low latitudes as the waves cross the basin before succumbing to instability (LP04), but westward phase propagation is also seen outside the latitude band from 20S to 20N. This likely reflects a 'leftover' portion of the flow following instability. If energy is transferred to a topographic mode with zero surface PV, then the surface flows with PV will remain. This separation has been described previously in turbulence simulations (LaCasce & Brink 2000). The resulting surface vortices are typically deformation scale, with less potential energy than the waves examined here. As such, instability is suppressed, allowing them to propagate over longer distances. Further work could shed light on the effect of instability of such eddies.

Topographic scattering has been seen previously, in turbulence simulations (Rhines 1977; Owens & Bretherton 1978; Treguier & Hua 1988; Treguier & McWilliams 1990; Zhang & Xie 2024; Pudig & Smith 2025) and in numerical stability calculations (LaCasce *et al.* 2019; Davies *et al.* 2021; Palóczy & LaCasce 2022). Scattering represents a 'direct cascade' of energy from mesoscale features (here, Rossby waves) to smaller scales. As such, it is likely important for the ocean energy budget. Scattering also has implications for numerical models, if energy is transferred to unresolved scales.

We examined stability over both monochromatic and narrow-band random bathymetry. The latter obscures topographic locking, particularly if the topography is isotropic. Realistic bathymetry exhibits anisotropy and moreover has basin-scale features (Goff & Jordan 1988; Goff & Arbic 2010). As the height spectrum varies as K^{-2}, the largest-amplitude features have the largest horizontal scales. This includes structures such as the mid-ocean ridges, with amplitudes of thousands of metres. Thus energy transfer to basin-scale features could well occur, a possibility that has not been considered previously (to our knowledge). This could also have implications for the large-scale energy budget, as topographically locked flows are more susceptible to bottom dissipation. However, the present results are based on the two-layer system. Further work is required to understand how topographic locking carries over with continuous stratification.

Acknowledgements. H.H. and J.H.L. acknowledge support from The Rough Ocean Project, and are grateful for comments from two anonymous reviewers.

Funding. This work was supported by the Research Council of Norway (grant no. NFR 302743).

Declaration of interests. The authors report no conflict of interest.

Data availability statement. The data and codes used for the paper are available on request from the authors.

https://doi.org/10.1017/jfm.2026.11482 Published online by Cambridge University Press

References

Ambrizzi, T., Hoskins, B.J. & Hsu, H.-H. 1995 Rossby wave propagation and teleconnection patterns in the austral winter. *J. Atmos. Sci.* **52** (21), 3661–3672.

Becker, J.M. & Salmon, R. 1997 Eddy formation on a continental slope. *J. Mar. Res.* **55**, 181–200.

Benilov, E.S. 2001 Baroclinic instability of two-layer flows over one-dimensional bottom topography. *J. Phys. Oceanogr.* **31** (8), 2019–2025.

Bobrovich, A.V. & Reznik, G.M. 1999 Planetary waves in a stratified ocean of variable depth. Part 2. Continuously stratified ocean. *J. Fluid Mech.* **388**, 147–169.

Brændshøi, J. 2018 Two-layer ocean flow over a bump topography. Master's thesis, University of Oslo.

Bretherton, F.P. & Haidvogel, D.B. 1976 Two-dimensional turbulence above topography. *J. Fluid Mech.* **78** (1), 129–154.

Carnevale, G. & Frederiksen, J. 1987*a* Nonlinear stability and statistical mechanics of flow over topography. *J. Fluid Mech.* **175**, 157–181.

Carnevale, G.F. & Frederiksen, J.S. 1987*b* Nonlinear stability and statistical mechanics of flow over topography. *J. Fluid Mech.* **175**, 157–181.

Chelton, D.B. & Schlax, M.G. 1996 Global observations of oceanic Rossby waves. *Science* **272** (5259), 234–238.

Chelton, D.B., Schlax, M.G. & Samelson, R.M. 2011 Global observations of nonlinear mesoscale eddies. *Prog. Oceanogr.* **91** (2), 167–216.

Cipollini, P., Cromwell, D., Challenor, P.G. & Raffaglio, S. 2001 Rossby waves detected in global ocean colour data. *Geophys. Res. Lett.* **28** (2), 323–326.

Clarke, A.J. & Buchanan, S. 2024 Why is the westward Rossby wave propagation from the California coast 'too fast'? *J. Phys. Oceanogr.* **54** (3), 767–782.

Constantinou, N.C. 2015 Formation of large-scale structures by turbulence in rotating planets. PhD thesis, National and Kapodistrian University of Athens.

Constantinou, N.C. & Young, W.R. 2017 Beta-plane turbulence above monoscale topography. *J. Fluid Mech.* **827**, 415–447.

Cummins, P.F. 1992 Inertial gyres in decaying and forced geostrophic turbulence. *J. Mar. Res.* **50** (4), 545–566.

Davies, J., Khatri, H. & Berloff, P. 2021 Linear stability analysis for flows over sinusoidal bottom topography. *J. Fluid Mech.* **911**, A33.

Davis, T.J., Radko, T., Brown, J.M. & Dewar, W.K. 2025 Rough topography and fast baroclinic Rossby waves. *Geophys. Res. Lett.* **52** (2), e2024GL112589.

De Szoeke, R.A. 1983 Baroclinic instability over wavy topography. *J. Fluid Mech.* **130** (1), 279–298.

Flierl, G.R. 1977 Simple applications of McWilliams' 'A note on a consistent quasigeostrophic model in a multiply connected domain'. *Dyn. Atmos. Oceans* **1** (5), 443–453.

Flierl, G.R., Malanotte-Rizzoli, P. & Zabusky, N.J. 1987 Nonlinear waves and coherent vortex structures in barotropic β-plane jets. *J. Phys. Oceanogr.* **17** (9), 1408–1438.

Fofonoff, N.P. 1955 Steady flow in a frictionless homogeneous ocean. *J. Mar. Res.* **13**, 254–263.

Fu, L.-L. & Flierl, G.R. 1980 Nonlinear energy and enstrophy transfers in a realistically stratified ocean. *Dyn. Atmos. Oceans* **4** (4), 219–246.

Galanti, E. & Tziperman, E. 2003 A midlatitude–ENSO teleconnection mechanism via baroclinically unstable long Rossby waves. *J. Phys. Oceanogr.* **33** (9), 1877–1888.

Gallet, B. 2024 Two-dimensional turbulence above topography: condensation transition and selection of minimum enstrophy solutions. *J. Fluid Mech.* **988**, A13.

Gill, A.E. 1974 The stability of planetary waves on an infinite beta-plane. *Geophys. Astrophys. Fluid Dyn.* **6** (1), 29–47.

Goff, J.A. & Arbic, B.K. 2010 Global prediction of abyssal hill roughness statistics for use in ocean models from digital maps of paleo-spreading rate, paleo-ridge orientation, and sediment thickness. *Ocean Model.* **32** (1–2), 36–43.

Goff, J.A. & Jordan, T.H. 1988 Stochastic modeling of seafloor morphology: inversion of sea beam data for second-order statistics. *J. Geophys. Res.: Solid Earth* **93** (B11), 13589–13608.

Griffa, A. & Salmon, R. 1989 Wind-driven ocean circulation and equilibrium statistical mechanics. *J. Mar. Res.* **47**, 457–492.

He, J. & Wang, Y. 2024 Multiple states of two-dimensional turbulence above topography. *J. Fluid Mech.* **994**, R2.

Held, I.M. 1975 Momentum transport by quasi-geostrophic eddies. *J. Atmos. Sci.* **32** (7), 1494–1497.

Holloway, G. 2008 Observing global ocean topostrophy. *J. Geophys. Res.: Oceans* **113** (C7), C07054.

https://doi.org/10.1017/jfm.2026.11482 Published online by Cambridge University Press

ISACHSEN, P.E., LACASCE, J.H. & PEDLOSKY, J. 2007 Rossby wave instability and apparent phase speeds in large ocean basins. *J. Phys. Oceanogr.* **37** (5), 1177–1191.
JOHNSTON, T.M.S., SJUR, A.L.P., ISACHSEN, P.E. & LACASCE, J.H. 2025 Eddy- and wind-driven circulation in the enclosed basins of the Norwegian Sea evaluated using a model and absolute geostrophic flow from Argo. *J. Geophys. Res.: Oceans* **130** (7), e2024JC021990.
JONES, S. 1978 Rossby wave interactions and instabilities in a rotating, two-layer fluid on a beta-plane. Part I: Resonant interactions. *Geophys. Astrophys. Fluid Dyn.* **11** (1), 289–322.
JONES, S. 1979 Rossby wave interactions and instabilities in a rotating, two-layer fluid on a beta-plane. Part II: Stability. *Geophys. Astrophys. Fluid Dyn.* **12** (1), 1–33.
JURY, M.R. 2018 South Indian Ocean Rossby waves. *Atmos.-Ocean* **56** (5), 322–331.
KAMENKOVICH, I.V. & PEDLOSKY, J. 1996 Radiating instability of nonzonal ocean currents. *J. Phys. Oceanogr.* **26** (4), 622–643.
KESSLER, W.S. 1990 Observations of long Rossby waves in the northern tropical Pacific. *J. Geophys. Res.: Oceans* **95** (C4), 5183–5217.
DE LA LAMA, M.S., LACASCE, J.H. & FUHR, H.K. 2016 The vertical structure of ocean eddies. *Dyn. Statist. Clim. Syst.* **1**, dzw001.
LACASCE, J.H. 1998 A geostrophic vortex over a slope. *J. Phys. Oceanogr.* **28** (12), 2362–2381.
LACASCE, J.H. 2000 Baroclinic Rossby waves in a square basin. *J. Phys. Oceanogr.* **30** (12), 3161–3178.
LACASCE, J.H. 2002 On turbulence and normal modes in a basin. *J. Mar. Res.* **60**, 431–460.
LACASCE, J.H. 2017 The prevalence of oceanic surface modes. *Geophys. Res. Lett.* **44** (21), 11–097.
LACASCE, J.H. & BRINK, K.H. 2000 Geostrophic turbulence over a slope. *J. Phys. Oceanogr.* **30** (6), 1305–1324.
LACASCE, J.H. & GROESKAMP, S. 2020 Baroclinic modes over rough bathymetry and the surface deformation radius. *J. Phys. Oceanogr.* **50** (10), 2835–2847.
LACASCE, J.H. & PEDLOSKY, J. 2004 The instability of Rossby basin modes and the oceanic eddy field. *J. Phys. Oceanogr.* **34** (9), 2027–2041.
LACASCE, J.H., ESCARTIN, J., CHASSIGNET, E.P. & XU, X. 2019 Jet instability over smooth, corrugated, and realistic bathymetry. *J. Phys. Oceanogr.* **49** (2), 585–605.
LACASCE, J.H., PALÓCZY, A. & TRODAHL, M. 2024 Vortices over bathymetry. *J. Fluid Mech.* **979**, A32.
LEONARD, B.P. 1979 A stable and accurate convective modelling procedure based on quadratic upstream interpolation. *Comput. Meth. Appl. Mech. Engng* **19** (1), 59–98.
LORENZ, E.N. 1972 Barotropic instability of Rossby wave motion. *J. Atmos. Sci.* **29** (2), 258–265.
MADDEN, R.A. 1979 Observations of large-scale traveling Rossby waves. *Rev. Geophys.* **17** (8), 1935–1949.
MARSHALL, J. & NURSER, G. 1986 Steady, free circulation in a stratified quasi-geostrophic ocean. *J. Phys. Oceanogr.* **16** (11), 1799–1813.
MCWILLIAMS, J.C. 1977 A note on a consistent quasigeostrophic model in a multiply connected domain. *Dyn. Atmos. Oceans* **1** (5), 427–441.
OSYCHNY, V. & CORNILLON, P. 2004 Properties of Rossby waves in the North Atlantic estimated from satellite data. *J. Phys. Oceanogr.* **34** (1), 61–76.
OWENS, W.B. & BRETHERTON, F.P. 1978 A numerical study of mid-ocean mesoscale eddies. *Deep Sea Res.* **25** (1), 1–14.
PALÓCZY, A. & LACASCE, J.H. 2022 Instability of a surface jet over rough topography. *J. Phys. Oceanogr.* **52** (11), 2725–2740.
PEDLOSKY, J. 1979 *Geophysical Fluid Dynamics*. Springer.
PLATZMAN, G.W. 1968 The Rossby wave. *Q. J. R. Meteorol. Soc.* **94** (401), 225–248.
PUDIG, M.P. & SMITH, K.S. 2025 Baroclinic turbulence above rough topography: the vortex gas and topographic turbulence regimes. *J. Phys. Oceanogr.* **55** (5), 611–630.
RADKO, T. 2019 Control of baroclinic instability by submesoscale topography. *J. Fluid Mech.* **882**, A14.
REZNIK, G.M. & TSYBANEVA, T.B. 1999 Planetary waves in a stratified ocean of variable depth. Part 1. Two-layer model. *J. Fluid Mech.* **388**, 115–145.
RHINES, P.B. 1977 The dynamics of unsteady currents. In *The Sea* (ed. M. Goldberg & S. O'Brien), vol. 6, pp. 189–318. Wiley.
RIVIÈRE, G. 2010 Role of Rossby wave breaking in the west Pacific teleconnection. *Geophys. Res. Lett.* **37**, L11802.
ROSSBY, C.-G. 1939 Relations between variations in the intensity of the zonal circulation of the atmosphere and the displacements of the semipermantent centers of action. *J. Mar. Res.* **2**, 38–55.
SALMON, R. 1978 Two-layer quasi-geostrophic turbulence in a simple special case. *Geophys. Astrophys. Fluid Dyn.* **10** (1), 25–52.

https://doi.org/10.1017/jfm.2026.11482 Published online by Cambridge University Press

SALMON, R. 1980 Baroclinic instability and geostrophic turbulence. *Geophys. Astrophys. Fluid Dyn.* **15** (1), 167–211.
SALMON, R., HOLLOWAY, G. & HENDERSHOTT, M.C. 1976 The equilibrium statistical mechanics of simple quasi-geostrophic models. *J. Fluid Mech.* **75** (4), 691–703.
SAMELSON, R.M. 1992 Surface-intensified Rossby waves over rough topography. *J. Mar. Res.* **50** (3), 367–384.
SIEGELMAN, L. & YOUNG, W.R. 2023 Two-dimensional turbulence above topography: vortices and potential vorticity homogenization. *Proc. Natl Acad. Sci. USA* **120** (44), e2308018120.
SOLODOCH, A., STEWART, A.L. & MCWILLIAMS, J.C. 2021 Formation of anticyclones above topographic depressions. *J. Phys. Oceanogr.* **51** (1), 207–228.
TAILLEUX, R. & MCWILLIAMS, J.C. 2001 The effect of bottom pressure decoupling on the speed of extratropical, baroclinic Rossby waves. *J. Phys. Oceanogr.* **31** (6), 1461–1476.
THEISS, J. 2004 Equatorward energy cascade, critical latitude, and the predominance of cyclonic vortices in geostrophic turbulence. *J. Phys. Oceanogr.* **34** (7), 1663–1678.
TREGUIER, A.M. & HUA, B.L. 1988 Influence of bottom topography on stratified quasi-geostrophic turbulence in the ocean. *Geophys. Astrophys. Fluid Dyn.* **43** (3–4), 265–305.
TREGUIER, A.M. & MCWILLIAMS, J.C. 1990 Topographic influences on wind-driven, stratified flow in a *eta*-plane channel: an idealized model for the Antarctic Circumpolar Current. *J. Phys. Oceanogr.* **20** (3), 321–343.
TSENG, K.-C., MALONEY, E. & BARNES, E. 2019 The consistency of MJO teleconnection patterns: an explanation using linear Rossby wave theory. *J. Climate* **32** (2), 531–548.
VALLIS, G.K. 2017 *Atmospheric and Oceanic Fluid Dynamics*. Cambridge University Press.
VANNESTE, J. 1995 Explosive resonant interaction of baroclinic Rossby waves and stability of multilayer quasi-geostrophic flow. *J. Fluid Mech.* **291**, 83–107.
VANNESTE, J. 2000 Rossby wave frequency change induced by small-scale topography. *J. Phys. Oceanogr.* **30** (7), 1820–1826.
VANNESTE, J. 2003 Nonlinear dynamics over rough topography: homogeneous and stratified quasi-geostrophic theory. *J. Fluid Mech.* **474**, 299–318.
VOET, G., QUADFASEL, D., MORK, K.A. & SØILAND, H. 2010 The mid-depth circulation of the Nordic Seas derived from profiling float observations. *Tellus A: Dyn. Meteorol. Oceanogr.* **62** (4), 516–529.
WANG, J. & VALLIS, G.K. 1994 Emergence of Fofonoff states in inviscid and viscous ocean circulation models. *J. Mar. Res.* **52**, 83–127.
ZANG, X. & WUNSCH, C. 1999 The observed dispersion relationship for North Pacific Rossby wave motions. *J. Phys. Oceanogr.* **29** (9), 2183–2190.
ZHANG, H. & WU, L. 2010 Predicting North Atlantic sea surface temperature variability on the basis of the first-mode baroclinic Rossby wave model. *J. Geophys. Res.: Oceans* **115** (C9), C09030.
ZHANG, L.-F. & XIE, J.-H. 2024 Spectral condensation and bidirectional energy transfer in quasi-geostrophic turbulence above small-scale topography. *Phys. Fluids* **36** (8), 086601.

https://doi.org/10.1017/jfm.2026.11482 Published online by Cambridge University Press